ACS APPLIED NANO MATERIALS

www.acsanm.org Article

Slowing Sintering to Increase the Lifetime of Cu Nanoparticles on Metal Oxide Supports

Fabio Rasera, Alisson S. Thill, Lívia P. Matte, Gustavo Z. Girotto, Helena V. Casara, Guilherme B. Della Mea, Naira M. Balzaretti, Fernanda Poletto, Carolina Brito, and Fabiano Bernardi*

Cite This: *ACS Appl. Nano Mater.* 2023, 6, 6435−6443 Read Online

ACCESS | Metrics & More | Article Recommendations | Supporting Information

ABSTRACT: The development of thermally stable nanoparticles is of utmost importance for applications like catalysis. In particular, Cu nanoparticles supported on metal oxides are easily deactivated under thermal treatments at low temperatures by sintering of the Cu nanoparticles. The formation of thermally stable nanoparticles is typically obtained with secondary drawbacks. In this study, an alternative method for avoiding sintering of Cu nanoparticles is proposed. The method is based on the impregnation of dithiol molecules at the metal oxide support before supporting the Cu nanoparticles. The dithiol molecules are able to avoid the Cu nanoparticle diffusion, thus decreasing the coalescence rate. Furthermore, the Cu nanoparticles are not poisoned during thermal treatments. A simple model is proposed and numerically studied to estimate the minimal concentration of dithiol necessary to avoid sintering of the nanoparticles. The method is not complex, and there is no interference on the original Cu nanoparticles properties. It opens possibilities for widening the lifespan of metal nanoparticles supported on metal oxides.

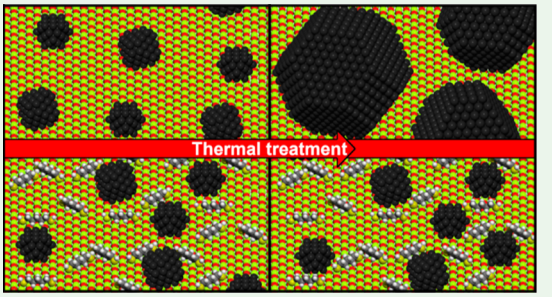

KEYWORDS: *sintering, Cu nanoparticles, poisoning, catalysis, dithiol*

INTRODUCTION

The wide use of nanoparticles nowadays is mainly driven by the size and shape dependence of the physical, electronic, and chemical properties.[1,2] In heterogeneous catalysis, the activity and selectivity of metallic nanoparticles supported on metal oxides have a strong dependence on the nanoparticle size[3] with a specific size for optimal performance. It occurs because the smaller the size, the higher the amount of low coordination sites, but, on the other hand, it induces a change in the orbital hybridization and charge transfer between nanoparticles and molecules, sometimes impairing the activity.[4]

The main drawback in applications using high temperatures (like catalysis) is the occurrence of sintering of the nanoparticles, then dramatically influencing the nanoparticle properties. For this reason, sintering is the predominant cause of catalyst deactivation,[5] shorting their lifespan to a few cycles or even to a single cycle. Sintering effects restrict the use of Cu nanoparticles in catalysis even for a low temperature of 300 °C.[6] A long and tedious search for a solution brought alternatives for this issue like coating of nanoparticles with oxide shells.[7] Recently, some authors made profit of the oxide capping layer coming from the support during the activation step of catalysts, traditionally known as the strong metal−support interaction effect, to immobilize the nanoparticles.[8] However, this inevitably covers part of the available surface, which is critical for catalysis applications. Even considering that the oxide capping layer from the support may improve the catalytic activity in some cases,[9] it may also deteriorate it,[10] and this strategy is not widely applied. Alternatively, it is possible to design porous supports for confining the nanoparticles.[11] In this case, some issues like pore collapse and the appearance of interconnectivity between pores are prone to happen at high temperatures, and they enable cluster and atomic migration.[12] A recent development was the use of nanoparticles fixed in zeolites.[13] It is a promising method for creating thermally stable nanoparticles, but the fixation of the nanoparticles in the porous support is currently restricted to noble-metal nanoparticles, and the application to other nanoparticles is still challenging.[14] Finally, alloying the nanoparticles with a second metal may increase the melting point, then increase the thermal stability, and, consequently, prevent sintering.[15] Cao and Veser synthesized a thermally stable nanocatalyst with a PtRh alloy.[16] The authors showed that the thermal stability of these nanoparticles depends critically on the Pt/Rh ratio, with higher Rh contents leading to increased thermal stability.[16] However, it changes the chemical and physical properties of the nanoparticles, and, in some cases, a thermally induced de-

Received: March 13, 2023
Accepted: March 21, 2023
Published: March 31, 2023

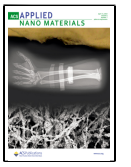

https://doi.org/10.1021/acsanm.3c01092
ACS Appl. Nano Mater. 2023, 6, 6435−6443

alloying process occurs.[17] In summary, simple and widely applied methods with no interference on the metallic nanoparticle properties are still missing. In this study, a new proposal to avoid sintering of nanoparticles, free of interference on the nanoparticle surface, and of easy preparation, is reported and successfully applied to Cu nanoparticles that are widely used in catalysis. A possible mechanism whereby the method prevents sintering is proposed.

EXPERIMENTAL SECTION

The Cu nanoparticles were synthesized according to the method described previously.[18] $CuCl_2{\cdot}2H_2O$ (Sigma-Aldrich, 99.99%) was used with 134 mg and 0.79 mmol, dissolved in 3 mL of BMI·BF_4 ionic liquid (prepared in accordance with the literature[19]), and stirred at room temperature for 15 min. After this, a solution of $NaBH_4$ (Sigma-Aldrich, >98%) with 296 mg and 7.9 mmol was dissolved in 3 mL of methanol (Sigma-Aldrich, >99.8%) and added to the mixture. The mixture turned black due to the formation of Cu nanoparticles, which were washed 3 times with methanol (Sigma-Aldrich, >99.8%) and 3 times with dichloromethane (Sigma-Aldrich, >99.8%). The nanoparticles were isolated by centrifugation (3500 rpm) and dried under reduced pressure.

The proposed strategy to avoid sintering consists of impregnating the clean surface of the MgO (Sigma-Aldrich, 99.99%) support with 1,5-pentanedithiol (Sigma-Aldrich, 96%) molecules with 9 mol %. The dithiol was impregnated by dissolving it in dichloromethane (Sigma-Aldrich, >99.8%) and dripping this solution on MgO (without Cu) under ultrasound bath for 30 s. The sample was left at room temperature during 48 h for the evaporation of dichloromethane. After this period, the Cu nanoparticles were supported with 12 wt % in relation to the MgO support, impregnated with dithiol (Cu/MgO + DT_5) or not (Cu/MgO), as shown in Figure 1.

The XRD data were acquired in a Siemens 500D conventional diffractometer operating at 40 kV and 17 mA with Cu Kα characteristic radiation (λ = 1.5405 Å). The measurements were carried out in a Bragg−Brentano geometry, with a range of 20−90°, 0.05° step size, and 0.4 s by point. The powder was sieved to a 48 μm grain size before the measurements.

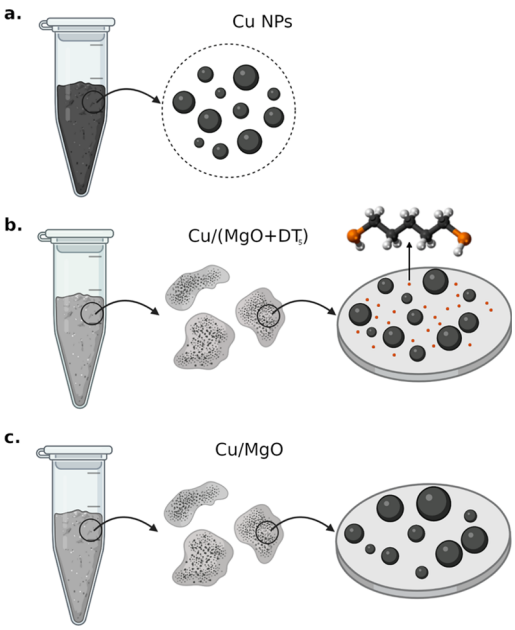

Figure 1. Illustration of the procedure used to avoid sintering of Cu nanoparticles. (a) Non-supported Cu nanoparticles, (b) Cu nanoparticles supported on MgO previously impregnated with 1,5-pentanedithiol (Cu/(MgO + DT_5)), and (c) Cu nanoparticles supported on MgO without dithiol impregnation (Cu/MgO).

The TEM images were acquired at CMM-UFRGS using a JEOL JEM 1200 Exll microscope operated at 80 kV and at Centro de Microscopia-UFMG using a Tecnai G2-12—SpiritBioTwin FEI operated at 120 kV. The nanoparticle powder was diluted in ethanol and dispersed using an ultrasound bath during 30 min. A drop of this solution was placed over a Cu grid coated by a thin C film.

In situ XAS measurements were performed at the Brazilian Synchrotron Light Source (LNLS) aiming the investigation of the local atomic order around Cu atoms and the time evolution of the oxidation state of Cu atoms of the Cu/MgO nanoparticles during the activation treatment. 55 mg of the nanoparticles powder was compacted to make a homogeneous 5 mm diameter pellet before introduction into the tubular furnace existing at the beamline. The gaseous atmosphere was introduced into the tubular furnace and went through the pellet, exiting at the opposite side to the exhaust system. The pellets are heated by a resistive heating system. The temperature at the sample holder is measured by a Chromel-Alumel thermocouple positioned at around 2 mm from the sample position. A power supply controls the sample temperature during the experiments with an accuracy of ±1 °C. The furnace has two external Kapton foil windows, allowing the in situ XAS measurements. This is valid for both in situ time-resolved XANES and in situ EXAFS measurements.

In situ time-resolved XANES measurements were carried out at the DXAS beamline at LNLS.[20] The measurements were performed at the Cu K edge (8979 eV) in a transmission mode. At the beginning, the Cu/MgO nanoparticles were exposed to 100 mL/min 5% H_2 + 95% He atmosphere. Then, the samples were heated subsequently to selected temperatures of 100, 200, 300, 400, and 500 °C with 10 °C/min heating rate. For each temperature, the sample was kept under H_2 atmosphere during 60 min. At the end, the H_2 atmosphere was removed, and the sample was exposed to 200 mL/min N_2 atmosphere and cooled to room temperature. The measurements made use of a curved Si(111) crystal (dispersive polychromator), which focuses the beam in the horizontal plane down to about 200 μm, a mirror that focuses it on the vertical plane to about 500 μm, and a position-sensitive CCD detector. The tubular furnace was placed in the beamline, taking care to place the pellet at the X-ray focal point. The time resolution of the measurements was around 100 ms.

In situ EXAFS measurements were carried out at the XAFS2 beamline at LNLS.[21] The measurements were conducted at the Cu K edge (8979 eV) in a transmission mode. The Cu/MgO nanoparticles were exposed to 100 mL/min 5% H_2 + 95% He atmosphere and heated to 300 °C with 10 °C/min heating rate. The nanoparticles remained at 300 °C with the H_2 atmosphere during 50 min. At the end, the H_2 atmosphere was removed, and the sample was exposed to 200 mL/min N_2 atmosphere and cooled to room temperature. The spectra were collected before and during reduction treatment at 300 °C using a Si(111) crystal and three ionization chambers. The samples were measured at room temperature and also at 300 °C, with the sample exposed to the reduction atmosphere. In this last case, measurement at 300 °C, the spectra were acquired after 50 min of sample exposure to the H_2 atmosphere at 300 °C in order to ensure the achievement of a steady state of the sample. A standard Cu foil was used to calibrate the Si(111) monochromator. Two to four scans were collected in order to improve the signal-to-noise ratio.

The XPS measurements were performed at the LNNano-CNPEM using a Thermo Scientific K-Alpha X-ray photoelectron spectrometer with an operating voltage of 12 kV and an Al Kα radiation source (1486.68 eV). The samples were measured before and after the reduction treatment at 300 °C performed during the in situ EXAFS measurements previously described. For the XPS measurements, a thin layer of powder was dispersed on a carbon tape. The base pressure used during the measurements was around 1×10^{-9} mbar. The photoelectrons were collected in the exit angle of 45° by a double focusing hemispherical analyzer operating in the CAE mode. To perform low- and high-resolution measurements, the pass energies used were 200 and 50 eV, while the energy steps were 1 and 0.1 eV, respectively, with a dwell time of 0.5 s. The measurements were

https://doi.org/10.1021/acsanm.3c01092
ACS Appl. Nano Mater. 2023, 6, 6435−6443

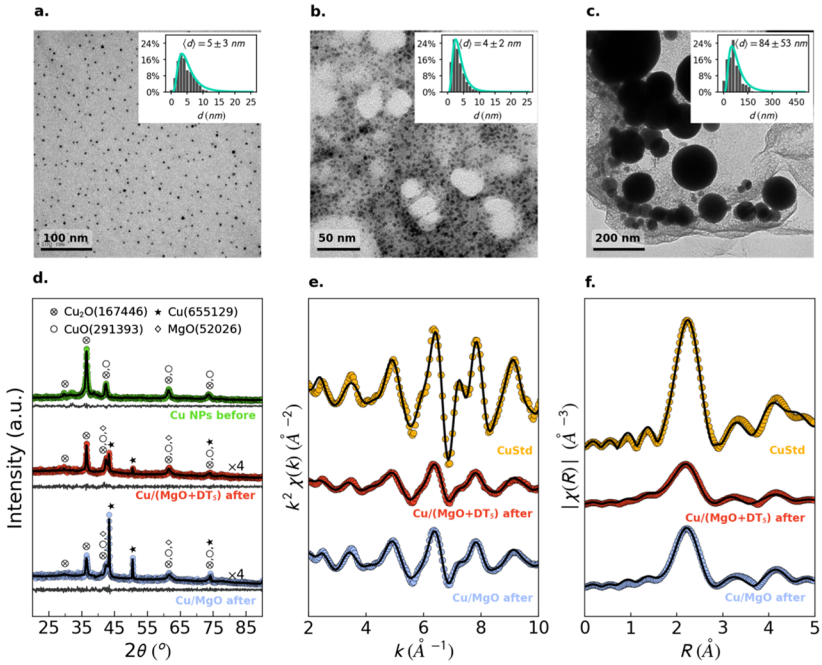

Figure 2. Typical TEM image of (a) non-supported Cu nanoparticles, (b) Cu/(MgO + DT_5), and (c) Cu/MgO nanoparticles after reducing treatment. The histogram of size distribution is shown in the inset. (d) XRD patterns of the as-prepared Cu (green), Cu/(MgO + DT_5) (red), and Cu/MgO (blue) nanoparticles after reducing treatment. The black and gray solid lines represent the Rietveld refinement result and the difference between data and fit, respectively. (e) In situ EXAFS oscillations and (f) corresponding Fourier transform of Cu standard (yellow), Cu/(MgO + DT_5) (red), and Cu/MgO (blue) during reducing treatment.

conducted in the long scan Cu 2p, S 2p, Mg 1s, O 1s, and C 1s electronic regions. The analyzer's energy calibration was performed using a standard Au foil (Au $4f_{7/2}$ peak at 84.0 eV). Charging effects in the samples were corrected using the C 1s position of adventitious carbon at 285.0 eV.

For the Fourier transform infrared spectroscopy (FTIR) measurements, about 1 mg of the nanoparticle powder was mixed with 100 mg of KBr powder, and this mixture was compacted to produce homogeneous pellets. The measurements were performed at room temperature using a FTIR spectrophotometer (Hartmann & Braun-Bomen) in a transmittance mode to obtain the FTIR spectra in the wavenumber range from 6500 to 450 cm^{-1}.

Data Analysis. The XRD patterns were indexed using the Crystallographica Search-Match software and the International Centre for Diffraction Data (ICDD) database. The FullProf software was used to conduct the Rietveld Refinement.[22] The background was modeled using a linear interpolation with adjustable parameters. As a peak profile, the Thompson−Cox−Hastings pseudo-Voigt convoluted with an axial divergence asymmetry function was used. Some parameters were fixed in the refinement: the atomic positions in the primitive cell, the occupation number, and the angle between the primitive vectors for each phase. Material anisotropy and preferential orientation were not included.

The TEM images were analyzed using the ImageJ software.[23] For each discernible cluster in an image, the mean Feret diameter was measured. To generate size distributions, around 2000 mean Feret diameters were used.

The in situ XAS data were analyzed in accordance with the standard procedure of data reduction[24] with the IFEFFIT package.[25] The analysis of the in situ time-resolved XANES spectra at the Cu K edge was performed using the linear combination of the Cu standard spectra measured in the energy range between −20 and +30 eV around the absorption edge. For the fit procedure, the XANES spectra of Cu^0, Cu_2O, CuO, and $CuSO_4$ standards were used. The weight of each component was constrained to positive values, and the sum of all contributions was set equal to 1.0.

The in situ EXAFS data were analyzed in accordance with the standard procedure of data reduction[24] with the IFEFFIT package.[25] The EXAFS signal $\chi(k)$ was extracted and then Fourier-transformed using a k^2-weighted $\chi(k)$ and a Kaiser−Bessel window with a k range of 9.0 $Å^{-1}$. The phase shift and amplitudes were obtained with the FEFF6 code. For the fit of the EXAFS oscillations, the amplitude reduction factor (S_0^2) was fixed at 0.85, as obtained from the Cu^0 standard fit. The R-factor obtained from the analysis was always lower than 0.03, which demonstrates the excellent agreement between the proposed model and the experimental result.

The XPS spectra were analyzed using the XPSPeak software. A Shirley-type background was used. The Au 4f region of an Au standard was analyzed in order to determine the pseudo-Voigt profile with 55% Lorentzian and 45% Gaussian contribution. The FWHM of a given chemical component and the relative binding energy of different components were constrained to be the same in all samples. Furthermore, the doublets, originating from spin orbit coupling, have their distances and area ratios fixed.

Numerical Section. We propose a mechanism to better understand the sintering process and a simplified model to predict how much dithiol compared to Cu nanoparticles is necessary to avoid sintering. In the model, Cu nanoparticles are supposed to diffuse in a surface which has fixed dithiol molecules.

Due to the presence of the obstacles, the nanoparticle diffusion coefficient D is affected by the pair coalescence to form more massive particles.[26,27] To simulate this mechanism, the nanoparticles were modeled as spherical random walkers constrained to walk over a 2D flat and inert surface that represents the MgO support. The dithiol molecules are represented by hard spheres that are randomly affixed at the support area and hereafter referred to as "obstacles". Nanoparticles jump lengths are sampled from an exponential distribution.[28,29]

$$\rho_i(s) = \frac{1}{\lambda_i} e^{-s/\lambda_i} \quad (1)$$

where s is the jump size and λ_i is a parameter that can be related to the particle size and the temperature. The nanoparticle jump is denied when the displacement results in a superposition with an obstacle, whereas if there is a superposition of two nanoparticles, they merge,

https://doi.org/10.1021/acsanm.3c01092
ACS Appl. Nano Mater. 2023, 6, 6435−6443

Table 1. Comparison between the Mean Diameters Obtained from Different Experimental Techniques

	TEM as-prepared (nm)	TEM after H_2 reduction (nm)	XRD as-prepared (nm)	XRD after H_2 reduction (nm)	EXAFS in situ (nm)
Cu nanoparticles	(5 ± 3)		(25 ± 15)		
Cu/(MgO + DT_5)	(5 ± 2)	(4 ± 3)		(26 ± 12)	(1.0 ± 0.2)
Cu/MgO		(84 ± 53)		(83 ± 26)	(2.1 ± 0.6)

conserving the mass and density. It follows from eq 1 that the average jump size of a particle is λ_i.

In the simulation we use $\lambda_i = \frac{K}{R_i^{3/2}}$, where $K = 1$ is a constant and R_i is the radius of the ith particle. To evaluate a time scale for the simulation, the Einstein−Smoluchowski relation[30] $D = \frac{\Delta^2}{2d\tau}$ was used, where Δ is the jump size, d is the number of dimensions, and τ the time step. Setting $\Delta = \lambda_0$, $d = 2$, and $D = D_0$, where λ_0 and D_0 are, respectively, the typical jump size and the diffusion coefficient of particles at the beginning of the simulation, gives $\tau = \frac{{\lambda_0}^2}{4D_0} = \frac{K^2}{4{R_0}^3 D_0}$, where R_0 stands for the mean nanoparticle radius at the beginning of the simulation.

A relevant parameter is the fraction of the substrate that is occupied by the projection of the initial number of nanoparticles N_{NP} and the number of obstacles N_O, called the initial occupation fraction ϕ_0 and defined as

$$\phi_0 = \frac{\pi}{L^2}(N_{NP}{R_{NP}}^2 + N_O{R_O}^2) \quad (2)$$

where R_{NP} is the nanoparticle initial radius, R_O is the obstacle radius, and L^2 is the total area of the substrate in the simulation. The experimental value of ϕ_0 in the samples was estimated to be around 0.2−0.4, with the N_2 adsorption−desorption isotherm measurements and the nanoparticle and dithiol masses in each sample.

RESULTS AND DISCUSSION

Figure 2a shows a typical TEM image of the Cu nanoparticles synthesized. The Cu nanoparticles are spherical and present a mean diameter of 5 ± 3 nm. A TEM image of the MgO support is shown in Figure S1 of the Supporting Information, where particles in the micrometer range are observed. The impregnation of Cu nanoparticles on the MgO support does not change the mean Cu nanoparticle size for both Cu/MgO and Cu/(MgO + DT5) nanoparticles, as demonstrated in Figure S2 of the Supporting Information. After thermal treatment (Figure 2b), the Cu/(MgO + DT_5) sample shows an increase of the nanoparticle density, however without changes in their shape and mean size in comparison to the as-prepared Cu nanoparticles. On the other hand, the same thermal treatment induces a strong sintering effect of the Cu nanoparticles (Table 1) with an increase of almost 17 times in the mean size in the sample without impregnation of dithiol molecules (Figure 2c). This result shows that the impregnation of dithiol in the support successfully prevents the sintering of Cu/(MgO + DT_5) nanoparticles.

The XRD pattern (Figure 2d) of the as-prepared Cu nanoparticles presents the CuO and Cu_2O phases, as expected.[18] The reducing treatment induces the presence of the metallic Cu phase, but the Cu_2O phase is still present due to atmosphere exposition. Since Cu_2O is the only phase of the Cu nanoparticles existing in both cases, this phase was used for comparison purposes of the crystallite size of the Cu nanoparticles obtained from Rietveld refinement. Again, the sample without dithiol impregnation presents a drastic growth of the mean diameter (see Table 1) after thermal treatment, corroborating the sintering behavior observed from TEM images. The Cu/(MgO + DT_5) nanoparticles maintain the same mean diameter of the Cu nanoparticles before thermal treatment, confirming sintering prevention.

Figure 2e,f shows the in situ EXAFS oscillations and the corresponding Fourier transform (FT) at the Cu K edge (8979 eV). The EXAFS oscillations of the samples during reduction treatment are clearly damped in comparison to the Cu standard measured at room temperature. It occurs due to the small size of the Cu nanoparticles and the high temperature of the measurements. Moreover, it is possible to observe damped EXAFS oscillations of the Cu/(MgO + DT_5) sample in comparison to the Cu/MgO one. Since both measurements were conducted at the same temperature (300 °C), it is further evidence of sintering prevention in the sample impregnated with dithiol. The same qualitative conclusion is obtained by analyzing the height of the Cu−Cu component from the coordination shell at FT. The average coordination number of the coordination shell is directly related to the nanoparticle size.[31] Using Calvin's model,[31] the nanoparticles size was estimated from in situ EXAFS analysis in Table 1. The results from all techniques follow the same size trend, corroborating that sintering occurred in the Cu/MgO sample, while it was prevented in the Cu/(MgO + DT_5) sample.

The differences found in the mean diameter values obtained from XRD and EXAFS in situ analysis in comparison to the TEM analysis occur because it is well known that the EXAFS technique is more sensitive to small crystallites, whereas XRD analysis is more sensitive to large crystallites.[31] Therefore, the diameters obtained from EXAFS represent an inferior limit in the mean size, while the diameters obtained by XRD point to a superior limit. For the nanoparticle size distribution from TEM, most of the counts are indeed inside these boundaries. As shown in Table 1, for all measurements, the Cu/MgO nanoparticles present the larger mean size after thermal treatment, clearly indicating sintering. Although EXAFS analysis does not give a size before the reducing treatment for comparison purposes due to the initial complex composition of the nanoparticles (see the XANES analysis discussion below), it shows that the Cu/(MgO + DT_5) nanoparticles have about half the size of the Cu/MgO nanoparticles during reduction treatment.

The strategy to avoid sintering of Cu nanoparticles was verified by three independent experimental techniques. This strategy greatly works for avoiding sintering due to the coalescence mechanism (nanoparticles weakly adhered to the support), but the same cannot be affirmed for sintering effects due to the Ostwald ripening mechanism (nanoparticles strongly adhered to the support).[32] For the coalescence mechanism, the method should be independent on the ligand used in the synthesis of the nanoparticles whether the intended application is catalysis since the ligands are removed before the catalytic reaction in the activation step. For other applications, it is expected that the presence of ligands at the nanoparticle surface would even help to avoid sintering of the nanoparticles since they are used as stabilizing agents.

Cu/(MgO + DT_5) nanoparticles were also prepared using half amount of dithiol and subjected to the same thermal

https://doi.org/10.1021/acsanm.3c01092
ACS Appl. Nano Mater. 2023, 6, 6435−6443

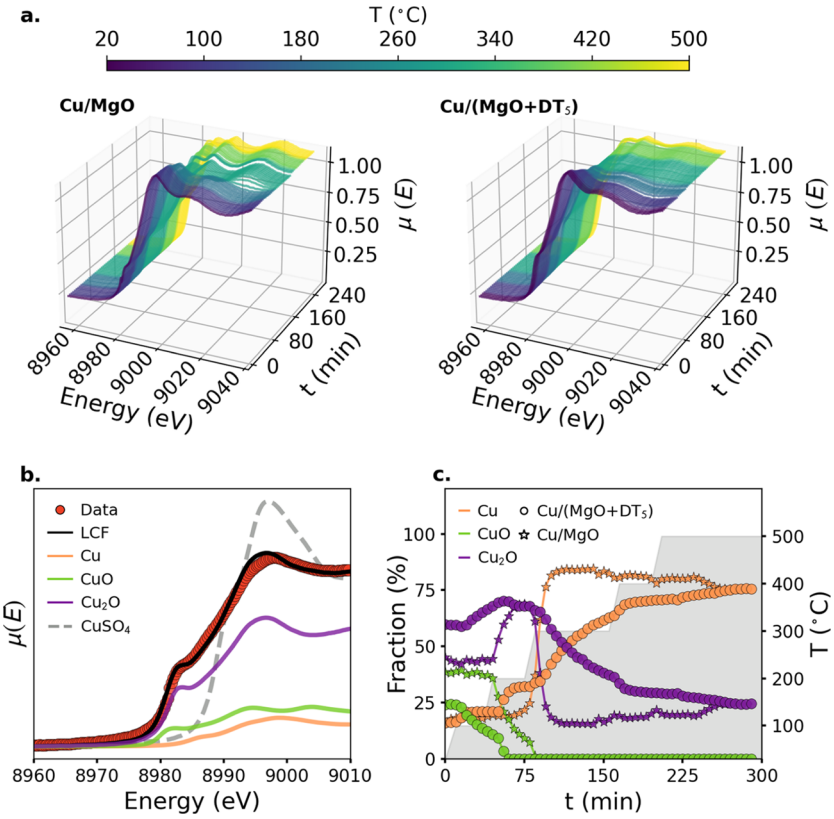

Figure 3. (a) In situ time-resolved XANES spectra at the Cu K edge of Cu/MgO and Cu/(MgO + DT_5) nanoparticles. The color scale represents the temperature during treatment. (b) Typical linear combination fit of a XANES spectrum of the Cu/(MgO + DT_5) sample at 300 °C. The solid lines represent the components used in the fit, and the dashed line represents the component with no contribution. (c) Time variation of Cu, CuO, and Cu_2O fractions during reduction treatment for Cu/(MgO + DT_5) (open circles) and Cu/MgO (open stars) nanoparticles obtained from in situ time-resolved XANES measurements. The solid gray step-like region describes the temperature variation, given by the right vertical axis.

treatment. TEM measurements (see Figure S3 of the Supporting Information) show almost the same mean particle size, demonstrating that half the amount of dithiol is enough to avoid sintering. Furthermore, the experiment was repeated using MgO impregnated with 1,3-propanedithiol or 1,4-butanedithiol molecules, and the same qualitative results were obtained, showing the robustness of the method (see Figures S4−S6 and Table S1 of the Supporting Information).

This proposal is useful even when no S poisoning of the nanoparticles is observed. A detailed in situ time-resolved XANES analysis was conducted aiming to identify a possible S poisoning and the time and temperature needed to poison the Cu nanoparticles. Figure 3a shows the in situ time-resolved XANES spectra during heating to 500 °C under H_2 atmosphere for both samples. Using a linear combination fit of several standards for the XANES spectra every 5 min (Figure 3b), the fractional composition of the samples as a function of time and temperature was obtained (Figure 3c). The XANES fingerprints of the as-prepared nanoparticles are consistent with the presence of mainly Cu(I) oxidation state.[33] During the reaction, the edge contribution becomes smaller, showing the reduction of Cu(I) to metallic Cu. At the end of the reduction treatment, the Cu nanoparticles are mainly in the metallic state (75%) with a Cu_2O contribution as well (25%). The $CuSO_4$ component shows very distinctive features that are not observed in the XANES spectra. The XANES spectra of CuS and Cu_2S show fingerprints different than those shown in Figure 3a.[34] Furthermore, there is no difference between the final XANES spectra of the Cu/MgO and Cu/MgO + DT_5 nanoparticles at 500 °C, besides the same signatures in the EXAFS oscillations (Figure 2e) and FT (Figure 2f) data. It shows the absence of sulfur poisoning of the Cu nanoparticles during reduction treatment. The change in the reduction kinetics of the Cu nanoparticles between both samples (Figure 3c) is probably associated with the preferential reduction of dithiol molecules at the MgO surface, which occurs before the Cu nanoparticle reduction, retarding the reduction of Cu nanoparticles in the Cu/(MgO + DTS) sample.

The Cu $2p_{3/2}$ XPS region (Figure 4a) exhibits two components at 932.8 and 934.5 eV, which are characteristic of Cu_2O[35] and CuO,[36] respectively. The presence of CuO after reduction treatment comes from oxidation due to atmosphere exposition. A $CuSO_4$ component is discarded since it is associated with a binding energy of 936.0 eV.[37] On the other hand, the Cu sulfide (Cu_xS) component is located at 932.5 eV,[38] overlapping with that of Cu_2O. However, if the Cu_xS component exists, it should appear in the S 2p XPS region as well.

Figure 4b shows the S 2p XPS region, where it is possible to observe the background noise for the Cu/MgO sample, as expected. The as-prepared Cu/(MgO + DT_5) sample presents two main components at 162.5 and 163.5 eV. The first one can be assigned to either Cu_xS or MgS_x[39] or can be even related to a Mg-SR^+ complex.[40] However, the S 2p binding energy in MgS_x ($1 \le x \le 2$) covers a wide range of possible values, from 163.5 eV for $x = 2$ to 161.5 eV for $x = 1$.[41,42] On the other hand, the S 2p binding energy of Cu_xS ($1 \le x \le 2$) typically does not vary so much with the oxidation state (<0.4 eV).[43]

https://doi.org/10.1021/acsanm.3c01092
ACS Appl. Nano Mater. 2023, 6, 6435−6443

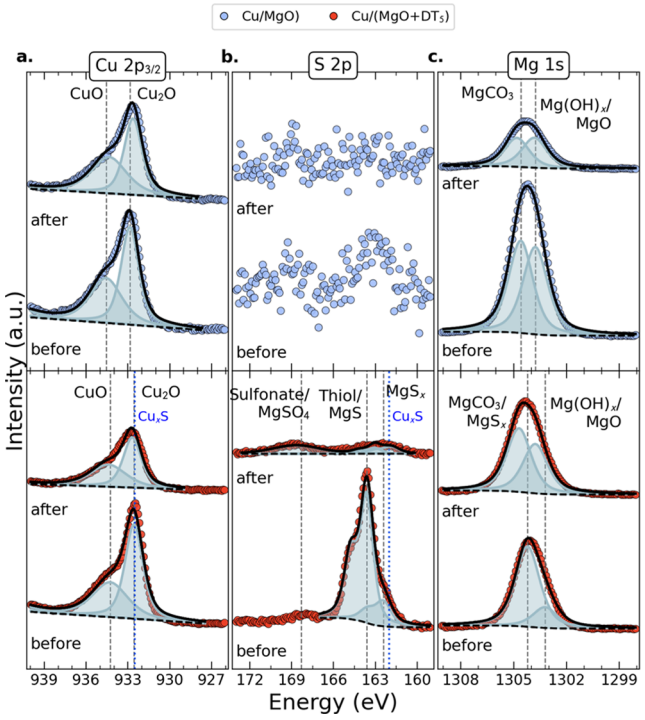

Figure 4. (a) Cu $2p_{3/2}$, (b) S 2p, and (c) Mg 1s XPS spectra of Cu/MgO (blue points) and Cu/(MgO + DT_5) (red points) nanoparticles before and after reducing treatment. The solid black lines represent the best fit found.

Thus, the large shift of 0.7 eV to smaller binding energy values of this component after reduction treatment suggests that it is not associated with a Cu_xS bond. In fact, the corresponding shift at Cu $2p_{3/2}$ is not observed. The possibility of S−S formation, which would have similar S 2p binding energy, is unlikely since at high temperatures, S−S cleaves in contact with transition metals.[44] On the other hand, a Mg surface interacting with S species typically contains multiple oxidation states;[41] therefore, both slightly and partially reduced S in MgS_x are probable. The component at 163.5 eV is associated with a thiol bond with a metal oxide[45] or even to unbounded thiol complexes.[46] After the reduction treatment, a new component was found at 169.0 eV, which was assigned to either sulfonate[45,46] or $MgSO_4$.[41] It is well known from the literature that thiol complexes oxidize to sulfonate when exposed to ambient atmosphere.[47,48] Therefore, the XPS spectra after reduction treatment suggest that a fraction of the dithiol molecules cleaved at high temperatures forming thiol complexes. Then the thiol complexes oxidize to sulfonate after exposure to ambient atmosphere and/or react forming $MgSO_4$.

These results are corroborated by the XPS analysis in the Mg 1s region (Figure 4c). The component at 1303.5 eV is associated with $Mg(OH)_x$ and/or MgO.[49] The component at 1304.5 eV is related to $MgCO_3$[50] and/or MgS_x.[42] It is usually the detection of MgO, $MgCO_3$, and $Mg(OH)_2$ simultaneously in the XPS analysis of MgO samples that is exposed to ambient atmosphere.[42] After the thermal treatment, a shift to a higher binding energy by 0.4 eV is observed for the MgS_x component. The energy shift direction agrees with the reducing of S atoms in MgS_x (Figure 3b). Then, the S bonding with the MgO support is clear instead of the poisoning of the Cu nanoparticles, where no binding energy shift in the Cu 2p region is observed (Figure 4a). It is important to stress out that Cu sulfides are stable under air exposition and only oxidation treatments at 350 °C are able to induce desorption of sulfide species;[51] then, a possible Cu sulfide formation is detected by XPS even after exposition of the sample to the atmosphere (prior to the XPS measurements). Furthermore, FTIR measurements were conducted, and, again, no Cu−S bonds were found in the nanoparticles (Figure S7 of the Supporting Information). A possible S poisoning of the Cu nanoparticles was also investigated for MgO impregnated with 1,3-propanedithiol or 1,4-butanedithiol molecules, but no evidence was found (Figures S8−S11 of the Supporting Information). The existing methods in the literature for avoiding sintering include (i) modification of the nanoparticle surface through the formation of a capping layer, which may impair the catalytic activity;[7] (ii) incorporation of nanoparticles inside pores,

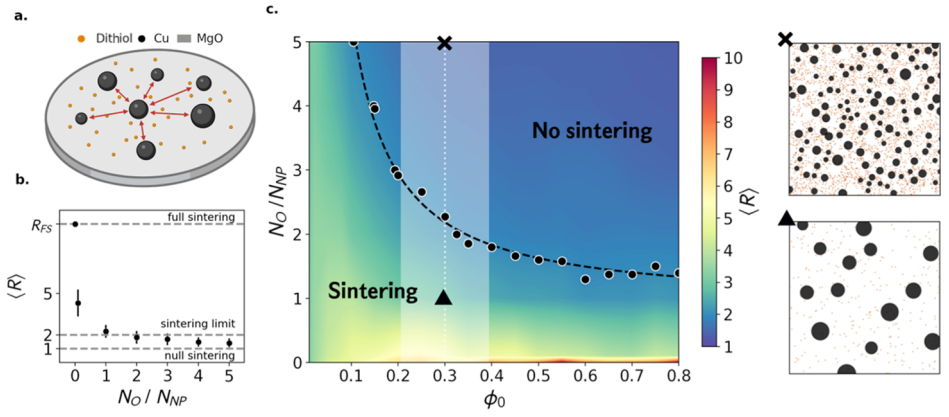

Figure 5. (a) Illustration of the sintering preventing mechanism. The dithiol molecules act as obstacles for the Cu nanoparticle diffusion. (b) Points represent the average particle sizes $\langle R \rangle$ (in units of R_{NP}), and bars represent the standard deviation as a function of the obstacle concentration N_O/N_{NP} for a simulation starting with $\phi_0 = 0.55$. "Full sintering" happens when there are no obstacles, and "null sintering" happens when coalescence is completely avoided. In between these two extremes, we set a "sintering limit" when $\langle R \rangle = 2R_{NP}$. (c) Diagram of the average particle size as a function of ϕ_0 and obstacle concentration N_O/N_{NP}. The black line indicates the sintering limit, separating a region where sintering is avoided from a region where nanoparticles coalesce. The white dashed line represents the experimental initial occupation fraction with its uncertainty given by the whitened zone around it. On the right there are two snapshots of the final configuration in the simulation for $N_O/N_{NP} = 1$ (triangle) and 5 (cross). The black dots represent Cu nanoparticles, and the orange dots represent dithiol molecules.

https://doi.org/10.1021/acsanm.3c01092
ACS Appl. Nano Mater. 2023, 6, 6435−6443

which is either complex or not widely applied for different systems;[11] and (iii) alloying the metal nanoparticle with a second metal, forming a bimetallic system with higher melting temperatures, which may also impair the catalytic activity since the surface is also changed.[14] The present study shows, in a pioneer way, a simple method for avoiding giant sintering effects without changes on the surface of the nanoparticles.

We now introduce a simplified model which allows us to estimate the proportion of dithiol molecules necessary to prevent the sintering of the nanoparticles. The model is based on the idea that the impregnation of dithiol molecules at the support decreases the Cu nanoparticle diffusion, preventing their sintering. The decrease in the diffusion of the nanoparticles is probably due to the presence of the dithiol that locally raises the activation energy for migration. Here, we mimic this mechanism by proposing the following model illustrated in Figure 5a: Nanoparticles are supposed to diffuse in a surface impregnated with fixed dithiol molecules that act as obstacles to the diffusion of the nanoparticles. We simulate this model numerically as explained in the "Numerical Section".

Figure 5 shows the results of the model. To study the influence of the dithiol in avoiding the nanoparticle coalescence, we vary systematically the concentration of obstacles, N_O/N_{NP}.

Figure 5b shows the average nanoparticle sizes $\langle R \rangle$ (in units of R_{NP}) as a function of N_O/N_{NP} for a simulation with ϕ_0 = 0.55. When there are no obstacles ($N_O/N_{NP} = 0$) and the time is long enough, all nanoparticles coalesce and form a unique sphere, indicated by the dashed line, called "full sintering". As the concentration of obstacles increases, $\langle R \rangle$ decreases monotonically until it reaches $\langle R \rangle \cong 1R_{NP}$ when N_O/N_{NP} = 5. This limit is identified as null sintering. We define that sintering happens when $\langle R \rangle = 2R_{NP}$, called the "sintering limit", which agrees with the experimental result (see Figure S3 of the Supporting Information). We then extend this analysis for all values of ϕ_0 (Figure 5c), showing a black line that divides two regimes: above the line, the concentration of obstacles is enough to avoid sintering. On the left of the diagram, snapshots of the system are presented with ϕ_0 = 0.3 and two situations: the situation below the dashed line where there are few obstacles ($N_O/N_{NP} = 1$) and sintering is not avoided. Black discs represent the Cu nanoparticles with an average radius of $\langle R \rangle$ = 2.8 R_{NP}, and orange points represent dithiol molecules. The snapshot above the dashed line shows an example where there are 5 times more dithiol particles compared to nanoparticles ($N_O/N_{NP} = 5$) which prevents its sintering. In this situation, $\langle R \rangle$ = 1.5 R_{NP}. In these figures, N_{NP} = 1000, R_{NP} = 2.5 nm, and $R_O = R_{NP}/10$. In the Supporting Information we show that our results are robust when we simulate bigger system sizes. The total simulation time is 10^5 Monte Carlo steps, which corresponds to 1 μs when the typical diffusion coefficient for Cu nanoparticles in the literature is considered.[52−54]

For ϕ_0 = 0.3, which is in the range of the value estimated experimentally for our samples, the model predicts that two times more obstacles than nanoparticles ($N_O/N_{NP} \approx 2$) would be required to avoid sintering. In the sample Cu/(MgO + DT_5), we estimate the concentration of dithiol molecules to be 5 times higher than the nanoparticles, suggesting that it has a concentration of dithiol well above the minimum concentration necessary to avoid coalescence of the nanoparticles, thus justifying why the present proposal is efficient in avoiding sintering.

In view of the above, it is proposed that the dithiol molecules bind to the MgO support through the formation of MgS_x bondings, as observed by XPS (Figure 4) and FTIR (Figure S7) analyses. It is important to stress out that the dithiol molecules were impregnated into the MgO support before the supporting process of Cu nanoparticles, which are not poisoned by the dithiol during thermal treatment, as determined from in situ XAS (Figures 2 and 3), XPS (Figure 4), and FTIR (Figure S7) analyses. The formation of MgS_x bondings allows the prevention of the sintering of Cu nanoparticles. The specific nature of the interaction that makes a dithiol molecule obstructing the migration path of a Cu nanoparticle is based on changing the local chemical environment of the support surface, which decreases nanoparticle diffusion by raising the activation energy for migration. In fact, it was already reported in the literature that the insertion of adatoms in fullerenes promotes its coalescence through a decrease of the activation energy.[55] On the other hand, this study reports on the dithiol molecules promoting the thermal stability of Cu nanoparticles by increasing the activation energy for coalescence and without poisoning the nanoparticles.

CONCLUSIONS

In this work, one of the greatest issues for nanoparticle applications was fixed using a pioneer proposal. The sintering of Cu nanoparticles is avoided using a simple preparation method and without covering the Cu nanoparticle surface or changing the physical−chemical properties of the nanoparticles. The impregnation of dithiol molecules at the support prevents sintering by hindering the Cu nanoparticle diffusion, probably by locally raising the activation energy for migration. Based on this mechanism, we proposed a simple model to estimate the minimal concentration of dithiol necessary to avoid sintering. Finally, the Cu nanoparticles are not poisoned by the dithiol molecules during high temperature thermal treatments, enabling their use in applications involving high temperature-like catalysis.

ASSOCIATED CONTENT

Supporting Information

The Supporting Information is available free of charge at https://pubs.acs.org/doi/10.1021/acsanm.3c01092.

Complementary TEM and FTIR results of the samples; experiments repeated for the MgO support impregnated with 1,3-propanedithiol and 1,4-butanedithiol molecules; and the corresponding results of TEM, XRD, in situ EXAFS, and in situ time-resolved XANES measurements (PDF)

AUTHOR INFORMATION

Corresponding Author

Fabiano Bernardi − *Programa de Pós-Graduação em Física, Instituto de Física, Universidade Federal do Rio Grande do Sul (UFRGS), Porto Alegre, Rio Grande do Sul 91501-970, Brazil;* orcid.org/0000-0001-6817-6860; Email: bernardi@if.ufrgs.br

Authors

Fabio Rasera − *Programa de Pós-Graduação em Física, Instituto de Física, Universidade Federal do Rio Grande do*

https://doi.org/10.1021/acsanm.3c01092
ACS Appl. Nano Mater. 2023, 6, 6435−6443

Sul (UFRGS), Porto Alegre, Rio Grande do Sul 91501-970, Brazil; orcid.org/0000-0001-8223-8079

Alisson S. Thill − *Programa de Pós-Graduação em Física, Instituto de Física, Universidade Federal do Rio Grande do Sul (UFRGS), Porto Alegre, Rio Grande do Sul 91501-970, Brazil*

Lívia P. Matte − *Programa de Pós-Graduação em Física, Instituto de Física, Universidade Federal do Rio Grande do Sul (UFRGS), Porto Alegre, Rio Grande do Sul 91501-970, Brazil*

Gustavo Z. Girotto − *Programa de Pós-Graduação em Física, Instituto de Física, Universidade Federal do Rio Grande do Sul (UFRGS), Porto Alegre, Rio Grande do Sul 91501-970, Brazil*

Helena V. Casara − *Programa de Pós-Graduação em Física, Instituto de Física, Universidade Federal do Rio Grande do Sul (UFRGS), Porto Alegre, Rio Grande do Sul 91501-970, Brazil*

Guilherme B. Della Mea − *Programa de Pós-Graduação em Física, Instituto de Física, Universidade Federal do Rio Grande do Sul (UFRGS), Porto Alegre, Rio Grande do Sul 91501-970, Brazil*

Naira M. Balzaretti − *Programa de Pós-Graduação em Física, Instituto de Física, Universidade Federal do Rio Grande do Sul (UFRGS), Porto Alegre, Rio Grande do Sul 91501-970, Brazil;* orcid.org/0000-0003-2797-8618

Fernanda Poletto − *Instituto de Química, Universidade Federal do Rio Grande do Sul (UFRGS), Porto Alegre, Rio Grande do Sul 91501-970, Brazil;* orcid.org/0000-0001-7217-0007

Carolina Brito − *Programa de Pós-Graduação em Física, Instituto de Física, Universidade Federal do Rio Grande do Sul (UFRGS), Porto Alegre, Rio Grande do Sul 91501-970, Brazil*

Complete contact information is available at: https://pubs.acs.org/10.1021/acsanm.3c01092

Author Contributions

The manuscript was written through contributions of all authors. All authors have given approval to the final version of the manuscript.

Notes

The authors declare no competing financial interest.

■ ACKNOWLEDGMENTS

This study was funded by the FAPERGS (project nos 19/2551-0001752-9 and 23/2551-0000177-2) and CAPES-Finance Code 001. F.R., A.S.T., L.P.M., G.Z.G., H.V.C., G.B.D.M., and F.B. thank the CNPq for the research grant (310142/2021-0). The authors also thank CMM-UFRGS, CM-UFMG, LNNano, and LNLS staff for their assistance.

■ REFERENCES

(1) Roduner, E. Size matters: Why nanomaterials are different. *Chem. Soc. Rev.* **2006**, *35*, 583−592.

(2) Matte, L. P.; Thill, A. S.; Lobato, F. O.; Novôa, M. T.; Muniz, A. R.; Poletto, F.; Bernardi, F. Reduction-driven 3D to 2D transformation of Cu nanoparticles. *Small* **2022**, *18*, 2106583.

(3) Xu, Z.; Xiao, F.-S.; Purnell, S. K.; Alexeev, O.; Kawi, S.; Deutsch, S. E.; Gates, B. C. Size-dependent catalytic activity of supported metal clusters. *Nature* **1994**, *372*, 346−348.

(4) Wang, H.; Lu, J. A Review on Particle Size Effect in Metal-Catalyzed Heterogeneous Reactions. *Chin. J. Chem.* **2020**, *38*, 1422−1444.

(5) Bartholomew, C. H. Mechanisms of catalyst deactivation. *Appl. Catal., A* **2001**, *212*, 17−60.

(6) Andrievski, R. A. Review of thermal stability of nanomaterials. *J. Mater. Sci.* **2014**, *49*, 1449−1460.

(7) Lee, S.; Seo, J.; Jung, W. Sintering-resistant Pt@CeO_2 nanoparticles for high-temperature oxidation catalysis. *Nanoscale* **2016**, *8*, 10219−10228.

(8) van Deelen, T. W.; Hernández Mejía, C.; de Jong, K. P. Control of metal-support interactions in heterogeneous catalysts to enhance activity and selectivity. *Nat. Catal.* **2019**, *2*, 955−970.

(9) Gesesse, G. D.; Wang, C.; Chang, B. K.; Tai, S.-H.; Beaunier, P.; Wojcieszak, R.; Remita, H.; Colbeau-Justin, C.; Ghazzal, M. N. A. A soft-chemistry assisted strong metal−support interaction on a designed plasmonic core−shell photocatalyst for enhanced photocatalytic hydrogen production. *Nanoscale* **2020**, *12*, 7011−7023.

(10) Figueiredo, W. T.; Escudero, C.; Pérez-Dieste, V.; Ospina, C. A.; Bernardi, F. Determining the Surface Atomic Population of Cu_xNi_{1-x}/CeO_2 ($0 < x \leq 1$) Nanoparticles during the Reverse Water−Gas Shift (RWGS) Reaction. *J. Phys. Chem. C* **2020**, *124*, 16868−16878.

(11) Liu, J.; Ji, Q.; Imai, T.; Ariga, K.; Abe, H. Sintering-resistant nanoparticles in wide-mouthed compartments for sustained catalytic performance. *Sci. Rep.* **2017**, *7*, 41773.

(12) Cao, A.; Lu, R.; Veser, G. Stabilizing metal nanoparticles for heterogeneous catalysis. *Phys. Chem. Chem. Phys.* **2010**, *12*, 13499−13510.

(13) Wang, L.; Xu, S.; He, S.; Xiao, F.-S. Rational construction of metal nanoparticles fixed in zeolite crystals as highly efficient heterogeneous catalysts. *Nano Today* **2018**, *20*, 74−83.

(14) Wang, L.; Wang, L.; Meng, X.; Xiao, F.-S. New Strategies for the Preparation of Sinter-Resistant Metal-Nanoparticle-Based Catalysts. *Adv. Mater.* **2019**, *31*, 1901905.

(15) Cao, A.; Lu, R.; Veser, G. Stabilizing metal nanoparticles for heterogeneous catalysis. *Phys. Chem. Chem. Phys.* **2010**, *12*, 13499−13510.

(16) Cao, A.; Veser, G. Exceptional high-temperature stability through distillation-like self-stabilization in bimetallic nanoparticles. *Nat. Mater.* **2010**, *9*, 75−81.

(17) Jeon, T.-Y.; Yoo, S. J.; Cho, Y.-H.; Kang, S. H.; Sung, Y.-E. Effect of de-alloying of Pt-Ni bimetallic nanoparticles on the oxygen reduction reaction. *Electrochem. Commun.* **2010**, *12*, 1796−1799.

(18) Matte, L. P.; Kilian, A. S.; Luza, L.; Alves, M. C. M.; Morais, J.; Baptista, D. L.; Dupont, J.; Bernardi, F. Influence of the CeO_2 Support on the Reduction Properties of Cu/CeO_2 and Ni/CeO_2 Nanoparticles. *J. Phys. Chem. C* **2015**, *119*, 26459−26470.

(19) Cassol, C. C.; Ebeling, G.; Ferrera, B.; Dupont, J. A simple and practical method for the preparation and purity determination of halide-free imidazolium ionic liquids. *Adv. Synth. Catal.* **2006**, *348*, 243−248.

(20) Cezar, J. C.; Souza-Neto, N. M.; Piamonteze, C.; Tamura, E.; Garcia, F.; Carvalho, E. J.; Neueschwander, R. T.; Ramos, A. Y.; Tolentino, H. C. N.; Caneiro, A.; Massa, N. E.; Martinez-Lope, M. J.; Alonso, J. A.; Itié, J.-P. Energy-dispersive X-ray absorption spectroscopy at LNLS: investigation on strongly correlated metal oxides. *J. Synchrotron Radiat.* **2010**, *17*, 93−102.

(21) Figueroa, S. J. A.; Mauricio, J. C.; Murari, J.; Beniz, D. B.; Piton, J. R.; Slepicka, H. H.; de Sousa, M. F.; Espíndola, A. M.; Levinsky, A. P. S. Upgrades to the XAFS2 beamline control system and to the endstation at the LNLS. *J. Phys.: Conf. Ser.* **2016**, *712*, 012022.

(22) Rodríguez-Carvajal, J. Recent advances in magnetic structure determination by neutron powder diffraction. *Phys. B* **1993**, *192*, 55−69.

(23) Schneider, C. A.; Rasband, W. S.; Eliceiri, K. W. NIH Image to ImageJ: 25 years of image analysis. *Nat. Methods* **2012**, *9*, 671−675.

(24) Koningsberger, D. C.; Prins, R. *X-ray Absorption: Principles, Applications, Techniques of EXAFS, SEXAFS, and XANES*; John Wiley & Sons, 1988.
(25) Ravel, B.; Newville, M. ATHENA, ARTEMIS, HEPHAESTUS: data analysis for X-ray absorption spectroscopy using IFEFFIT. *J. Synchrotron Radiat.* **2005**, *12*, 537−541.
(26) Gruber, E. E. Calculated size distributions for gas bubble migration and coalescence in solids. *J. Appl. Phys.* **1967**, *38*, 243−250.
(27) Harris, P. J. F. Growth and structure of supported metal catalyst particles. *Int. Mater. Rev.* **1995**, *40*, 97−115.
(28) Tsong, T. T. Experimental studies of the behaviour of single adsorbed atoms on solid surfaces. *Rep. Prog. Phys.* **1988**, *51*, 759−832.
(29) Lakatos-Lindenberg, K.; Shuler, K. E. Random walks with nonnearest neighbor transitions. I. Analytic 1-D theory for next-nearest neighbor and exponentially distributed steps. *J. Math. Phys.* **1971**, *12*, 633−652.
(30) Reichl, L. E.; Luscombe, J. H. A Modern Course in Statistical Physics, 2nd Edition. *Am. J. Phys.* **1999**, *67*, 1285−1287.
(31) Calvin, S.; Miller, M. M.; Goswami, R.; Cheng, S. F.; Mulvaney, S. P.; Whitman, L. J.; Harris, V. G. Determination of crystallite size in a magnetic nanocomposite using extended x-ray absorption fine structure. *J. Appl. Phys.* **2003**, *94*, 778−783.
(32) Jose-Yacaman, M.; Gutierrez-Wing, C.; Miki, M.; Yang, D.-Q.; Piyakis, K. N.; Sacher, E. Surface diffusion and coalescence of mobile metal nanoparticles. *J. Phys. Chem. B* **2005**, *109*, 9703−9711.
(33) Figueiredo, W. T.; Della Mea, G. B.; Segala, M.; Baptista, D. L.; Escudero, C.; Pérez-Dieste, V.; Bernardi, F. Understanding the Strong Metal-Support Interaction (SMSI) Effect in Cu_xNi_{1-x}/CeO_2 ($0 < x < 1$) Nanoparticles for Enhanced Catalysis. *ACS Appl. Nano Mater.* **2019**, *2*, 2559−2573.
(34) Kumar, P.; Nagarajan, R.; Sarangi, R. Quantitative X-ray absorption and emission spectroscopies: electronic structure elucidation of Cu_2S and CuS. *J. Mater. Chem. C* **2013**, *1*, 2448−2454.
(35) Vasquez, R. P. Cu_2O by XPS. *Surf. Sci. Spectra* **1998**, *5*, 257−261.
(36) Vasquez, R. P. CuO by XPS. *Surf. Sci. Spectra* **1998**, *5*, 262−266.
(37) Vasquez, R. P. $CuSO_4$ by XPS. *Surf. Sci. Spectra* **1998**, *5*, 279−284.
(38) Krylova, V.; Andruleviçius, M. Optical, XPS and XRD studies of semiconducting copper sulfide layers on a polyamide film. *Int. J. Photoenergy* **2009**, *2009*, 304308.
(39) Fantauzzi, M.; Elsener, B.; Atzei, D.; Rigoldi, A.; Rossi, A. Exploiting XPS for the identification of sulfides and polysulfides. *RSC Adv.* **2015**, *5*, 75953−75963.
(40) Soares, J. W.; Steeves, D. M.; Singh, J.; Im, J.; Whitten, J. E. Thiol adsorption on metal oxides: an approach for selective deposition on zinc oxide nanoparticles. *Oxide-based Materials and Devices II*; SPIE, 2011; Vol. *7940*, p 79400K.
(41) Gao, T.; Noked, M.; Pearse, A. J.; Gillette, E.; Fan, X.; Zhu, Y.; Luo, C.; Suo, L.; Schroeder, M. A.; Xu, K.; Lee, S. B.; Rubloff, G. W.; Wang, C. Enhancing the Reversibility of Mg/S Battery Chemistry through Li^+ Mediation. *J. Am. Chem. Soc.* **2015**, *137*, 12388−12393.
(42) Gao, T.; Hou, S.; Huynh, K.; Wang, F.; Eidson, N.; Fan, X.; Han, F.; Luo, C.; Mao, M.; Li, X.; Wang, C. Existence of Solid Electrolyte Interphase in Mg Batteries: Mg/S Chemistry as an Example. *ACS Appl. Mater. Interfaces* **2018**, *10*, 14767−14776.
(43) Kutty, T. R. N. A controlled copper-coating method for the preparation of ZnS: Mn DC electroluminescent powder phosphors. *Mater. Res. Bull.* **1991**, *26*, 399−406.
(44) Bain, C. D.; Biebuyck, H. A.; Whitesides, G. M. Comparison of Self-Assembled Monolayers on Gold: Coadsorption of Thiols and Disulfides. *Langmuir* **1989**, *5*, 723−727.
(45) Volmer, M.; Stratmann, M.; Viefhaus, H. Electrochemical and electron spectroscopic investigations of iron surfaces modified with thiols. *Surf. Interface Anal.* **1990**, *16*, 278−282.
(46) Bensebaa, F.; Zhou, Y.; Deslandes, Y.; Kruus, E.; Ellis, T. H. XPS study of metal-sulfur bonds in metal-alkanethiolate materials. *Surf. Sci.* **1998**, *405*, L472−L476.
(47) Laibinis, P. E.; Whitesides, G. M.; Allara, D. L.; Tao, Y. T.; Parikh, A. N.; Nuzzo, R. G. Comparison of the Structures and Wetting Properties of Self-Assembled Monolayers of n-Alkanethiols on the Coinage Metal Surfaces, Cu, Ag, Au. *J. Am. Chem. Soc.* **1991**, *113*, 7152−7167.
(48) Siriwardane, R. V.; Poston, J. A., Jr.; Fisher, E. P.; Shen, M. S.; Miltz, A. L. Decomposition of the sulfates of copper, iron (II), iron (III), nickel, and zinc: XPS, SEM, DRIFTS, XRD, and TGA study. *Appl. Surf. Sci.* **1999**, *152*, 219−236.
(49) Khairallah, F.; Glisenti, A.; Natile, M. M.; Galenda, A. ZnO/MgO Nanocomposites by Wet Impregnation: An XPS study. *Surf. Sci. Spectra* **2010**, *17*, 76−86.
(50) Khairallah, F.; Glisenti, A. XPS Study of MgO Nanopowders Obtained by Different Preparation Procedures. *Surf. Sci. Spectra* **2006**, *13*, 58−71.
(51) Galtayries, A.; Bonnelle, J. P. XPS and ISS Studies on the Interaction of H_2S with Polycrystalline Cu, Cu_2O and CuO Surfaces. *Surf. Interface Anal.* **1995**, *23*, 171−179.
(52) Kart, H. H.; Yildirim, H.; Ozdemir Kart, S.; Çagin, T. Physical properties of Cu nanoparticles: A molecular dynamics study. *Mater. Chem. Phys.* **2014**, *147*, 204−212.
(53) Yang, D. Q.; Sacher, E. Coalescence kinetics of copper clusters on highly oriented pyrolytic graphite and Dow Cyclotene, as determined by x-ray photoelectron spectroscopy. *J. Appl. Phys.* **2001**, *90*, 4768−4771.
(54) Hoehne, K.; Sizmann, R. Volume and surface self-diffusion measurements on copper by thermal surface smoothing. *Phys. Status Solidi* **1971**, *5*, 577−589.
(55) Lee, I.-H.; Jun, S.; Kim, H.; Kim, S. Y.; Lee, Y. Adatom-assisted structural transformations of fullerenes. *Appl. Phys. Lett.* **2006**, *88*, 011913.

https://doi.org/10.1021/acsanm.3c01092
ACS Appl. Nano Mater. 2023, 6, 6435−6443